Supplementary Information (SI) for Green Chemistry.

Supplementary Information for

Dielectric layer induces depolarization field and interfacial interaction evolution to stabilize Zn anode

Yiqun Du,*[a] Anbin Hu,[a] Huidi Shi,[a] Ning Li,[a] Yang Zhou[a], Jinkai Li,[a] and Bingqiang Cao*[a]

[a] School of Material Science and Engineering, Shandong Provincial Key Laboratory of Photovoltaic Materials and High-efficiency Utilization Technology, University of Jinan, Jinan, China

E-mail: mse_duyq@ujn.edu.cn, mse_caobq@ujn.edu.cn

1. Experimental Procedures

Preparation of NNO@Zn electrode: Commercial $NaNbO_3$ (NNO, Macklin) was used as received. A slurry was prepared by dispersing 90 mg of NNO and 10 mg of polyvinylidene fluoride (PVDF) in an appropriate volume of N-methyl-2-pyrrolidone (NMP). The slurry was then coated onto polished Zn foil using a four-sided wet film applicator, where the film thickness was regulated by selecting different coating sides. The electrodes were subsequently dried to obtain the final NNO-coated Zn anodes.

Preparation of MnO2 electrode: MnO_2 was synthesized by reacting $MnSO_4 \cdot H_2O$ (1 mmol) and $KMnO_4$ (6 mmol) in deionized water (50 mL) within a Teflon-lined autoclave at 150 °C for 24 hours. After washing and drying the product at 60 °C, a cathode slurry comprising MnO_2, carbon black, and PVDF (8:1:1 wt%) in NMP was coated onto stainless steel foil, achieving a mass loading of ~2 mg cm^{-2}.

Electrochemical measurements: Coin cells were assembled using bare Zn or NNO@Zn electrodes (14 mm diameter, 100 µm thickness), corresponding counter electrodes, glass fiber separators, and 100 µL of electrolyte. For Zn||MnO_2 cells, 0.1 M $MnSO_4$ was added to the electrolyte to suppress Mn^{2+} dissolution. Tafel curves were acquired on a CHI 660e workstation at 1 mV s^{-1} using a three-electrode setup (Zn working/counter, Ag/AgCl reference). Linear sweep voltammetry (LSV) was conducted at 5 mV s^{-1} using a Ti foil working electrode and graphite rod counter electrode. Battery cycling performance was evaluated using a Neware CT-4008Q testing system.

Characterizations: Raman spectra were collected on a Horiba HR Evolution spectrometer. Crystal structures were characterized by XRD (SmartLab) using Cu Kα radiation. SEM and AFM images were obtained with a GeminiSEM 360 and a Dimension Icon system, respectively. For ex situ analysis, Zn electrodes were harvested from Zn||Zn symmetric cells after 100 hours of cycling at 0.5 mA cm^{-2}/0.5 mAh cm^{-2} or 5 mA cm^{-2}/5 mAh cm^{-2}. In situ optical imaging of deposition process on 100 µm Zn foils was conducted using an Mshot MJ31 microscope.

Theoretical calculations: DFT calculations were performed using the PBE-GGA functional, a 450 eV plane-wave cutoff, and a 2×2×1 *k*-point grid. Convergence was achieved when energy and force residuals fell below 10^{-6} eV and 0.02 eV/Å, respectively. Binding energy was defined as $E_b = E(A + B) - E(A) - E(B)$. The Gibbs free energy of desolvation was evaluated at 298 K according to $\Delta G = \Delta E + \Delta E_{ZPE} + T\Delta S$, encompassing electronic energy (ΔE), zero-point energy (ΔE_{ZPE}), and entropic terms (ΔS).

Multiphysics simulations. The zinc deposition process was simulated using the tertiary current distribution model coupled with the Nernst–Planck equations. The top and bottom boundaries of the model were defined as the cathode and anode, respectively, while the left and right boundaries were treated as insulating boundaries. Electrode reaction kinetics were calculated using the Butler–Volmer equation, and ion diffusion was determined via the Nernst–Einstein relation. The initial Zn^{2+} concentration was set to 2 M, and the exchange current density was set to 1 mA cm^{-2}. For the coated-electrode model, the relative dielectric constant of the NNO dielectric layer was set to 35, whereas the bare Zn case was simulated in the absence of the dielectric interphase. The temporal evolution of the system was calculated using a transient solver.

2. Supporting Figures and Tables

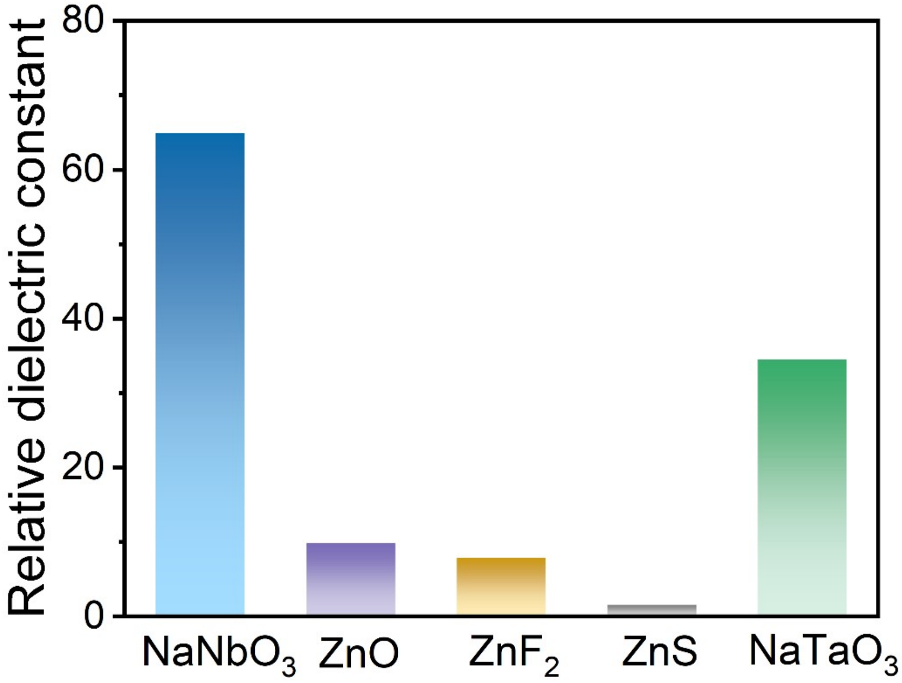

Figure S1. Relative dielectric constants of various artificial interphases.

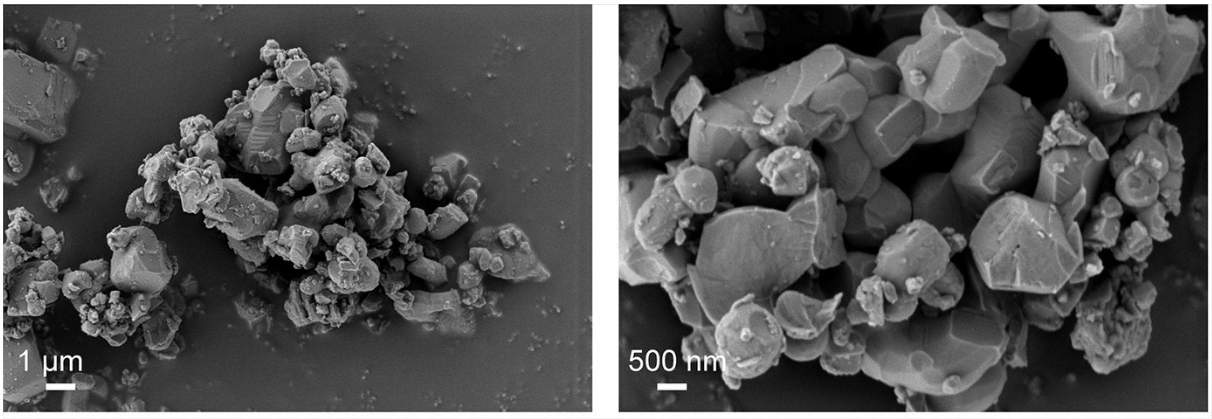

Figure S2. SEM images of the NNO powder.

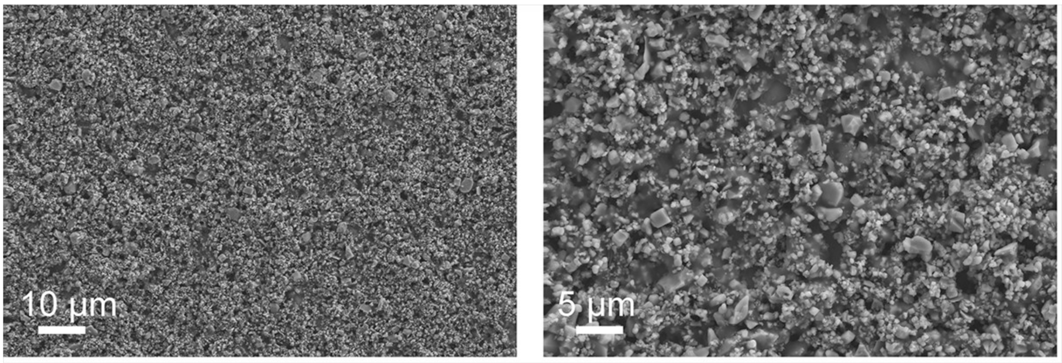

Figure S3. SEM images of the NNO@Zn interphase.

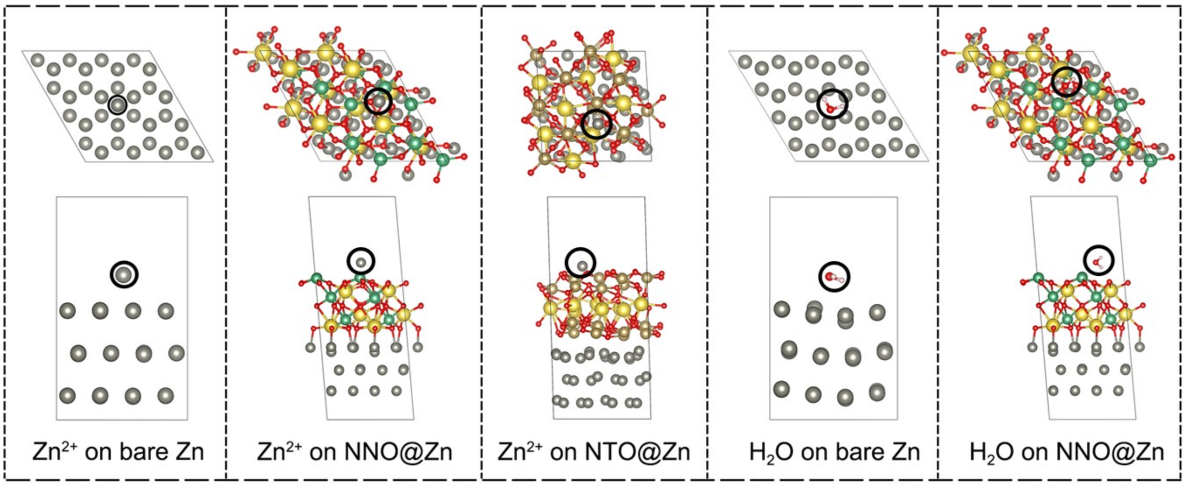

Figure S4. The adsorption sites of Zn^{2+} and H_2O for bare Zn, NNO@Zn, and NTO@Zn.

Both the bare Zn electrode and the NNO surface were modeled using the (002) facet.

For the bare Zn surface, the adsorbed Zn^{2+} was placed at a threefold hollow site on the Zn metal surface, whereas the H_2O molecule was molecularly adsorbed at an atop Zn site, adopting a slightly tilted off-top Zn-top configuration after structural optimization. For the NNO@Zn model, the H_2O molecule was molecularly adsorbed near an exposed surface Nb site on the NNO surface, exhibiting a tilted Nb-top configuration, while the adsorbed Zn^{2+} was located at an O-top site on the NNO surface. For the NTO@Zn model, the adsorbed Zn^{2+} was located at a threefold hollow site formed by surface oxygen atoms on the NTO surface.

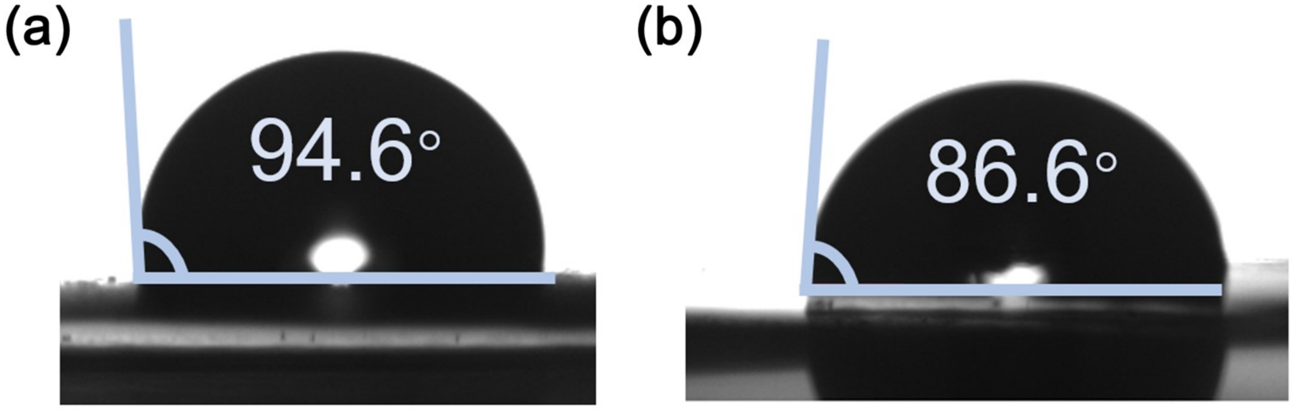

Figure S5. Contact angles of (a) bare Zn and (b) NNO@Zn electrodes.

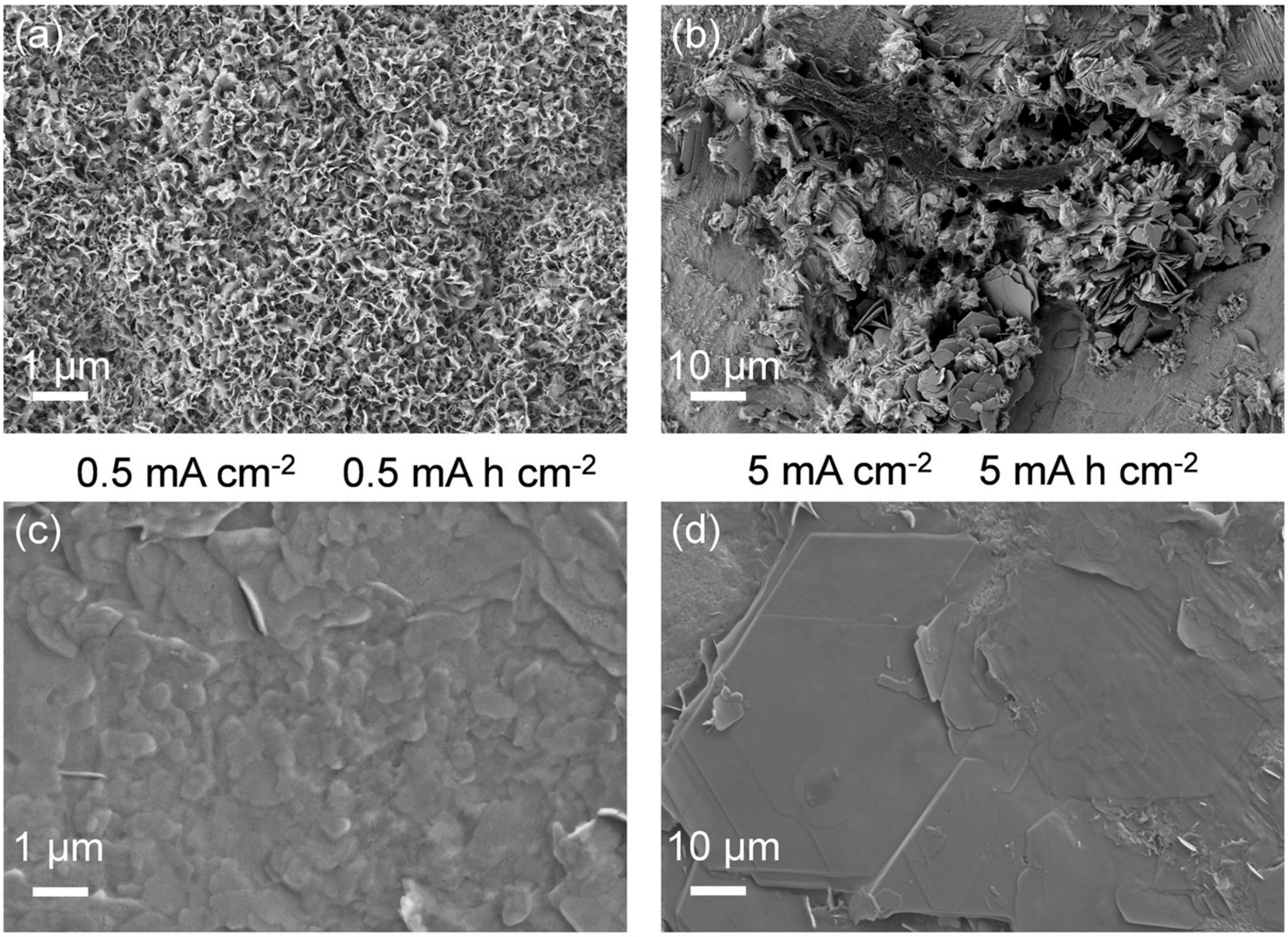

Figure S6. SEM images of bare Zn electrodes at (a) 0.5 mA cm^{-2}/0.5 mAh cm^{-2} and (b) 5 mA cm^{-2}/5 mAh cm^{-2} after cycling for 100 h. SEM images of 10NNO@Zn electrodes at (c) 0.5 mA cm^{-2}/0.5 mAh cm^{-2} and (d) 5 mA cm^{-2}/5 mAh cm^{-2} after cycling for 100 h.

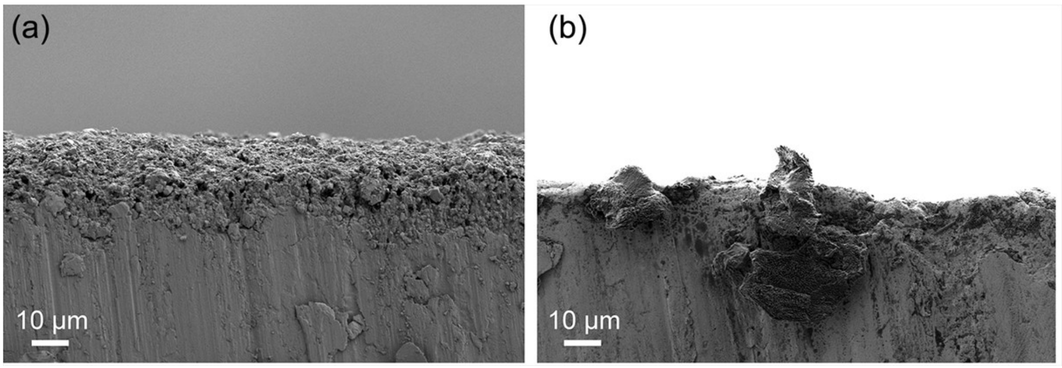

Figure S7. Cross-sectional SEM images for the (a) bare Zn and (b) 10NNO@Zn electrodes after deposition at 5 mA cm^{-2}/5 mAh cm^{-2}.

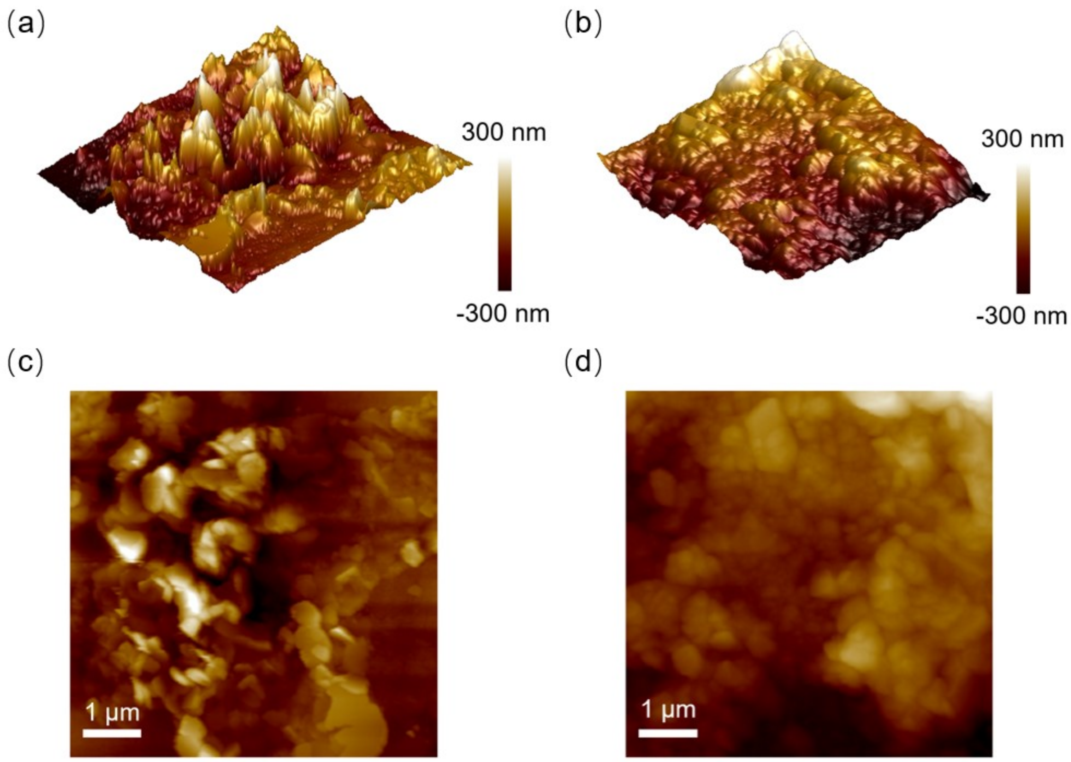

Figure S8. AFM images of (a, c) bare Zn and (b, d) 10NNO@Zn electrodes after cycling for 100 h at 0.5 mA cm^{-2}/0.5 mAh cm^{-2}.

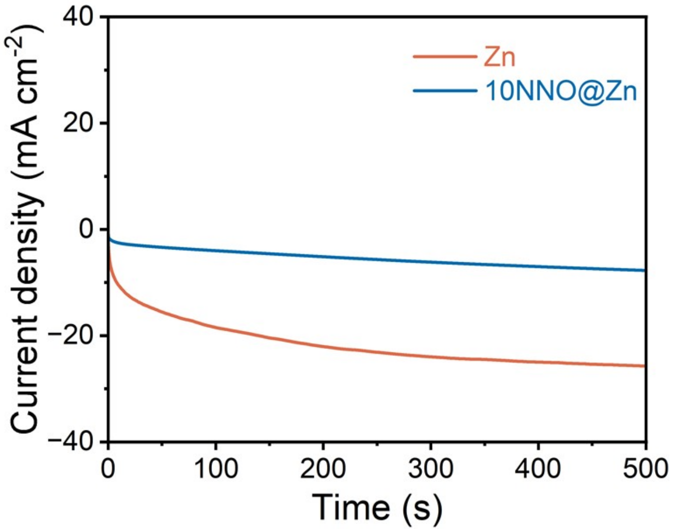

Figure S9. Chronoamperometry curves of diverse Zn electrodes.

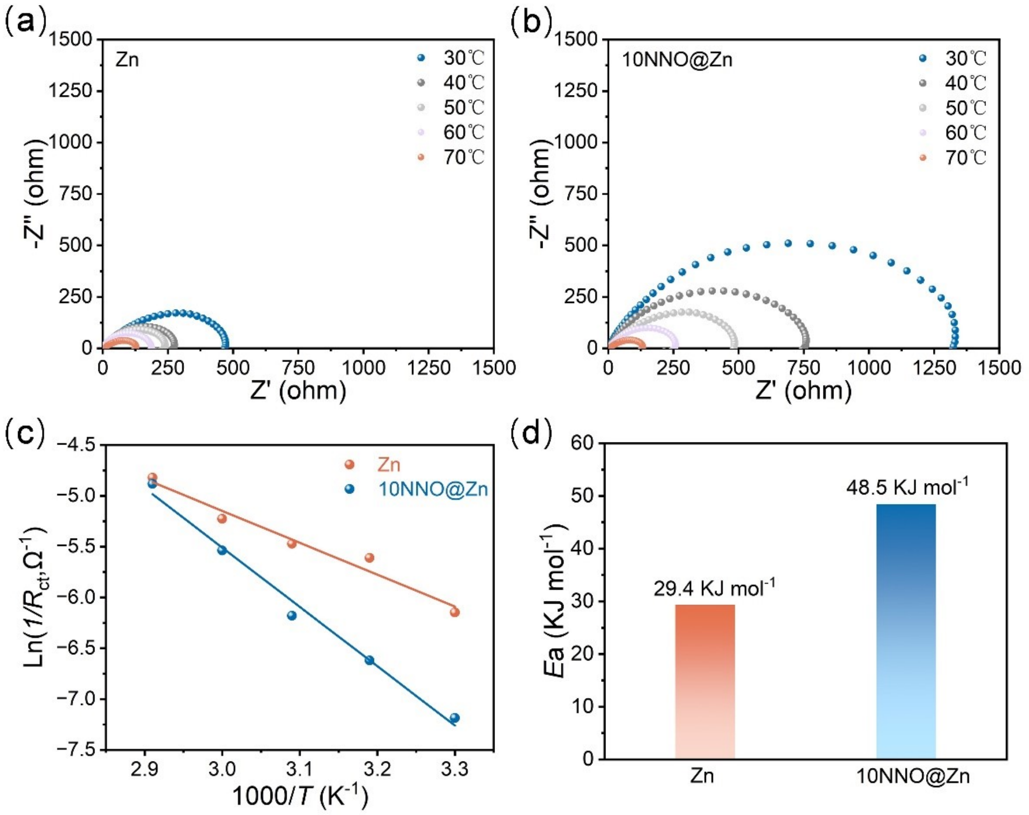

Figure S10. Nyquist plots for (a) bare Zn and (b) 10NNO@Zn electrodes. (c) Arrhenius plots. (d) Corresponding activation energies.

Activation energy (E_a) was calculated according to the Arrhenius relationship, $1/R_{ct} = A\exp(-E_a/RT)$, where R_{ct}, A, R and T denote the charge transfer resistance, pre-exponential factor, molar gas constant, and absolute temperature, respectively.

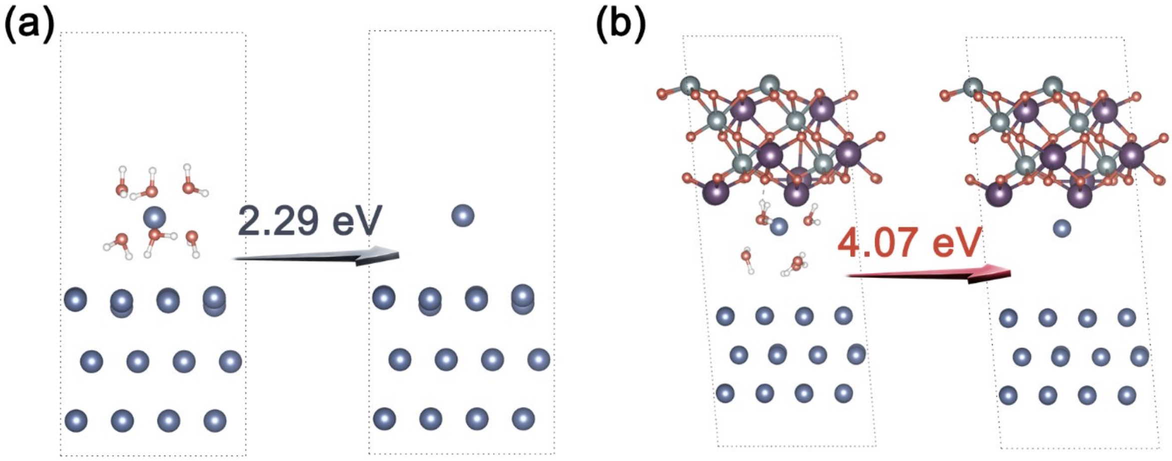

Figure S11. The models and corresponding Gibbs free energy of $[Zn(H_2O)_6]^{2+}$ desolvation on (a) bare Zn and (b) NNO@Zn electrodes.

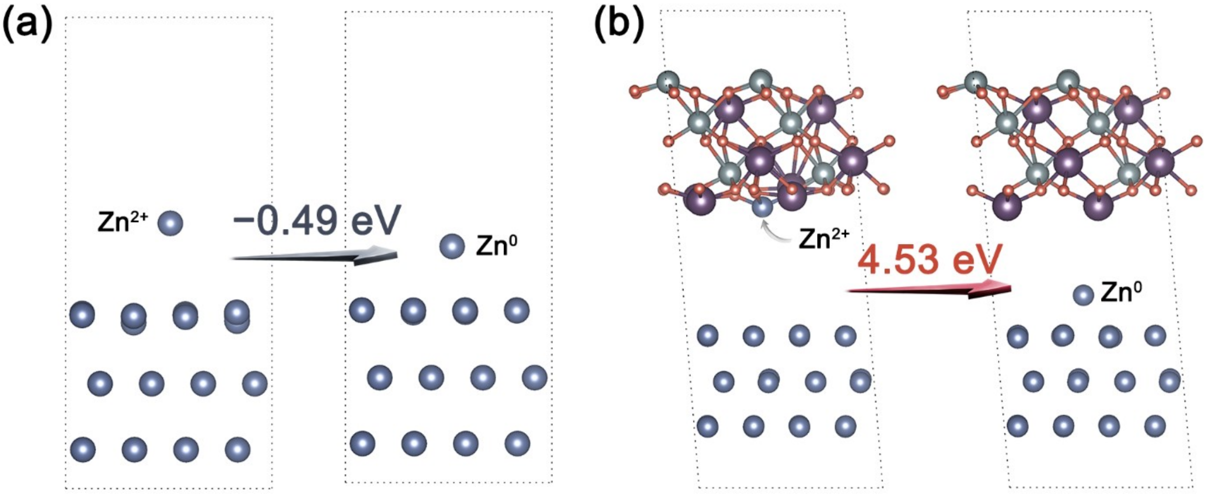

Figure S12. The models and Gibbs free energy for Zn^{2+} reduction on (a) bare Zn and (b) NNO@Zn electrodes.

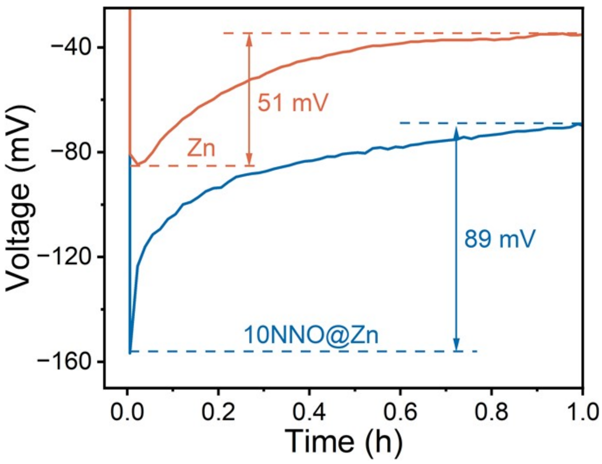

Figure S13. Nucleation overpotential of bare Zn and 10NNO@Zn electrodes.

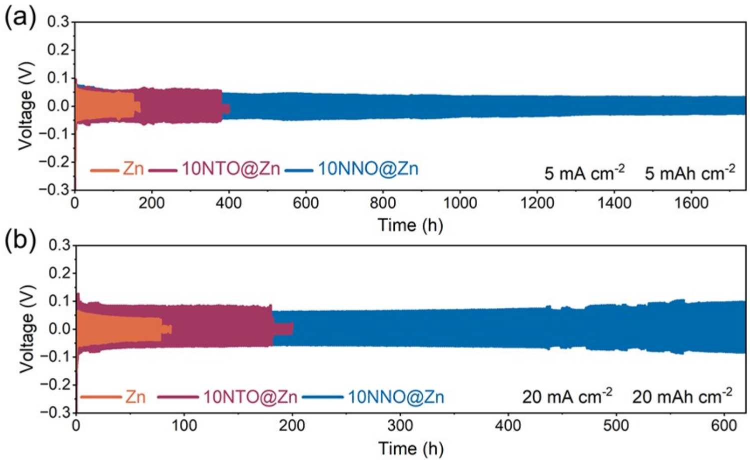

Figure S14. Voltage-time profiles of Zn||Zn cells at (a) 5/5 and (b) 20/20 mA cm^{-2}/mAh cm^{-2}.

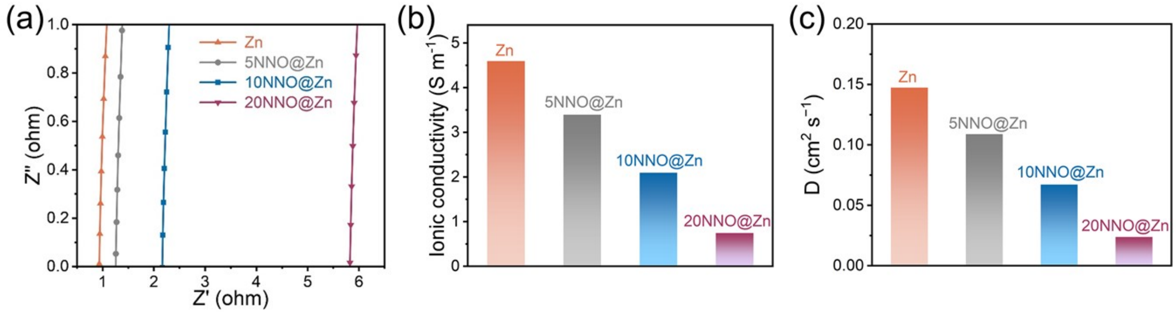

Figure S15. (a) EIS plots, (b) ionic conductivity, and (c) diffusion coefficients for various electrodes.

Note: The Zn^{2+} diffusion coefficients (D) were evaluated via the Nernst–Einstein relation. In the equation $D=\sigma RT/(n^2F^2C)$, σ represents the bulk ionic conductivity derived from electrochemical impedance spectroscopy, $n=2$ for Zn^{2+} ions, and C is the molar concentration of Zn^{2+} in the bulk electrolyte.

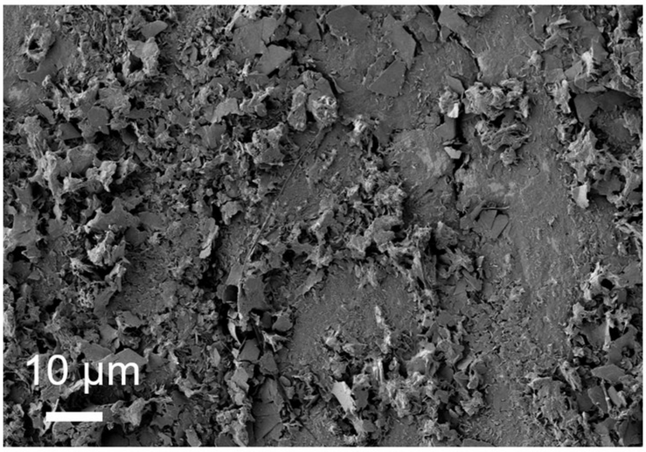

Figure S16. SEM image of the 20NNO@Zn electrode after cycling for 100 h at a current density of 0.5 mA cm^{-2}.

Table S1. Detailed cycling stability comparison of Zn||Zn batteries with diverse coating systems.

Electrode	Current density (mA cm^{-2})	Capacity (mA h cm^{-2})	Cycling stability (hours)	Reference
$NaNbO_3$@Zn	**0.5**	**0.5**	**3700**	**This work**
	5	**5**	**1700**	
	20	**20**	**615**	
$NiTiO_3$@Zn	2	1	2400	1
	5	1	2100	
	8	2	1800	
Zn@PANI	3	1.5	500	2
Cs_2TeI_6	1	1	2000	3
$ZnMoO_4$@Zn	2	2	2000	4
	5	5	1600	
	10	10	250	
$ZnNb_2O_6$@Zn	1	1	2000	5
	10	10	1000	
Zn-PDPTT	2	2	1380	6
P-CD@Zn	10	10	600	7
ZHP@Zn	1	1	1000	8
	5	2.5	750	
	10	2	250	
Zn@PCN-S	1	1	1500	9
	5	3	500	
	10	10	100	

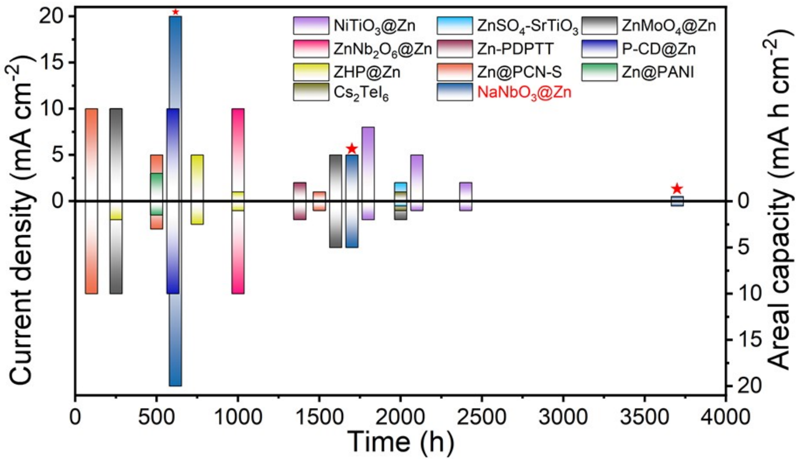

Figure S17. Comparison of the cycling stability among Zn batteries with various artificial interphases.

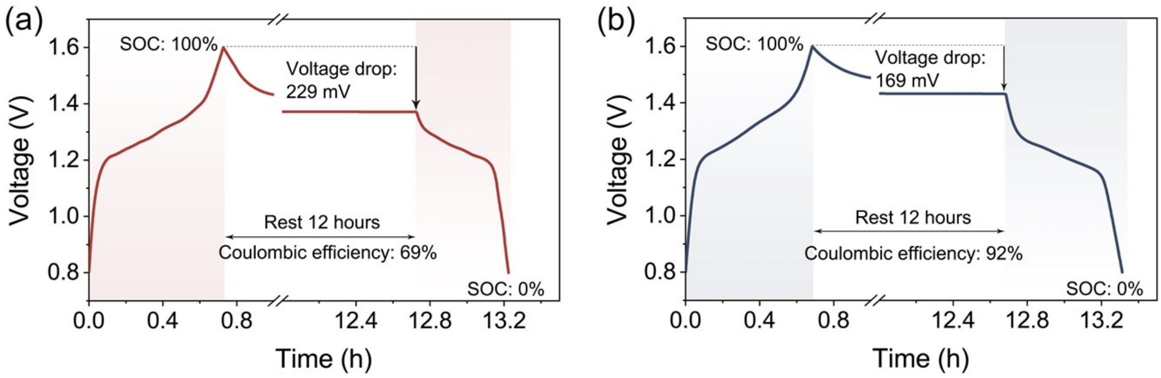

Figure S18. Voltage profiles with 12 h rest between charge and discharge for zinc−iodine batteries with (a) bare Zn and (b) 10NNO@Zn anodes.

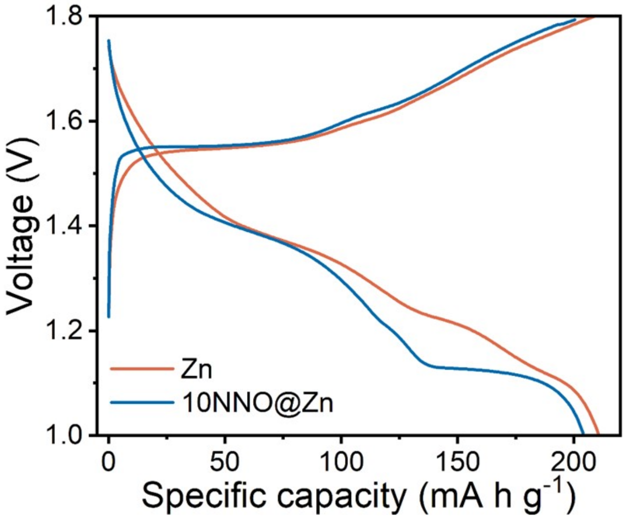

Figure S19. Charge-discharge curve of the Zn||MnO$_2$ batteries for the first cycle.

Reference

1. Y. Jin, X. Rao, H. Yang, J. Qin, X. Yang, D. Zhang, D. Luo, X. Zhang, J. Qin and J. Cao, *Chemical Engineering Journal*, 2025, **518**.
2. B. Li, S. Liu, Y. Geng, C. Mao, L. Dai, L. Wang, S. C. Jun, B. Lu, Z. He and J. Zhou, *Advanced Functional Materials*, 2023, **34**.
3. J. Li, C. Lei, P. Jiang, C. Xu, T. Liu and X. Liang, *Energy & Environmental Science*, 2024, **17**, 8633-8642.
4. A. Chen, C. Zhao, J. Gao, Z. Guo, X. Lu, J. Zhang, Z. Liu, M. Wang, N. Liu, L. Fan, Y. Zhang and N. Zhang, *Energy & Environmental Science*, 2023, **16**, 275-284.
5. H. Yang, J. Wang, P. Zhang, X. Cheng, Q. Guan, J. Dong, B. Chen, L. Jia, J. Zhang, Y. Zhang, Y. Liu and H. Lin, *Journal of Energy Chemistry*, 2025, **100**, 693-701.
6. M. Chen, X. Guo, X. Jiang, B. Farhadi, X. Guo, Y. Zhu, H. Zhang and S. Liu, *Angewandte Chemie International Edition*, 2024, **63**.
7. G. Zhang, L. Fu, Y. Chen, K. Fan, C. Zhang, H. Dai, L. Guan, H. Guo, M. Mao and C. Wang, *Angewandte Chemie International Edition*, 2024, **63**.
8. X. Qian, L. Li, Y. Wang, Z. Tian, H. Zhong, W. Chen, T. Chen and J. Fu, *Energy Storage Materials*, 2023, **58**, 204-214.
9. L. Han, Q. Wang, R. Pang, D. Zhang, B. Zhao, W. Meng, M. Li, Y. Zhang, A. Cao and Y. Shang, *Advanced Energy Materials*, 2023, **13**.